Hindawi
Journal of Sensors
Volume 2021, Article ID 4852313, 10 pages
https://doi.org/10.1155/2021/4852313

Research Article

Observation of Clinical Efficacy of Parylene-Coated Occluder Based on Electronic Image of Visual Sensor in the Treatment of Congenital Heart Disease

Hongdu Fu, Liming Liang, Huangwei Zhuang, and Jiahui Yang

Department of Cardiac Surgery, Central South University Xiangya School of Medicine Affiliated Haikou Hospital, Haikou, 570208 Hainan, China

Correspondence should be addressed to Huangwei Zhuang; zhuanghuangwei@stu.cpu.edu.cn

Received 19 June 2021; Revised 14 August 2021; Accepted 7 September 2021; Published 12 October 2021

Academic Editor: Haibin Lv

With the acceleration of people's life rhythm, the incidence of congenital heart disease is getting higher and higher. This study mainly explores the clinical efficacy observation of parylene-coated occluders based on the electronic image of the visual sensor in the treatment of congenital heart disease. The patient takes a supine position and observes whether the target structure (left ventricular cavity) information is separated from the capture area during rotation, and the angle of the probe is adjusted to ensure that as much target structure information as possible can be obtained during the two-dimensional image acquisition. During the three-dimensional ultrasound sampling process, a total of 60 coaxial images were collected within the range of 180°. To reflect the effect of virtual reality, it is necessary to provide users with interactive operation tools. This research provides two methods, mouse interaction and keyboard interaction. Through these two methods, the effect of the basic virtual endoscope is realized. Xtion's image registration process is completed inside its PS1080 system-level chip, and all sensor information, color images, and depth images are transmitted to the user host through the USB interface. For example, the point of view can be placed in the heart, because the simulation occlusion must first find a suitable section to better observe and judge the occlusion effect. Therefore, this study uses the mouse interaction method to change the cutting by dragging and rotating the mouse. In the process of releasing the occluder, the parylene-coated occluder can be released after the X-ray and ultrasound examination results are satisfactory, and the delivery long sheath and catheter can be sprinkled and compressed to stop the bleeding. During the operation, the ASD measured by two-dimensional ultrasound after balloon inflation was 24.17 ± 7.94 mm, and the anterior and posterior diameter was 21.30 ± 6.54 mm. This research is helpful for the qualitative and quantitative diagnosis of congenital heart disease.

1. Introduction

ASD is one of the most common congenital heart diseases and is dominated by secondary pores. The interventional treatment technology of using a cardiac catheterization device to block the secondary port ASD has replaced complicated thoracic surgery to a certain extent. The effect of applying parylene occluder in the treatment of secondary port ASD has been affirmed, and a wealth of clinical experience has been accumulated.

In addition, from the imaging point of view, the parylene-coated occluder can assist doctors in locating the lesion more clearly and understand the patient's condition; the study of assessing the degree of aortic constriction from CT images can increase the diagnostic value of CT images.

Incorporating genetic risk information into electronic health records (EHR) will help implement genomic medicine in clinical practice. Brown et al. believe that little is known about patients' attitudes towards using genetic risk information as part of personal health information in EHR. Their research investigated whether the disclosure of the genetic risk score (GRS) of coronary heart disease affects people's attitudes towards including personal health information including genetic risk in the EHR. Combine CRS

and GRS into EHR, and make it available to patients and doctors. Data from 2013 to 2015 were collected and analyzed in 2015-2016. Participants of GRS and CRS in their study reported positive attitudes towards the experiment, but the research process was too cumbersome [1]. Purnima and El-Aal conducted a study on the Wadi Al Dawasir (K.S.A) population aged 20-80 through random sampling from October 2012 to June 2013. It includes 250 samples, and these cases are classified as diabetes and hypertension. In this case, pure hypertension was 52, diabetes was 57, and the mixed group included 65 patients with diabetes and hypertension. Fasting blood was collected to analyze lipid distribution. Their research only gives the content of the investigation and lacks comparative data [2]. Pan et al. believe that dexmedetomidine reduces cardiac complications in adults undergoing cardiovascular surgery. He evaluated whether perioperative dexmedetomidine can improve the surgical outcome of a patient with congenital heart disease (CHD). They searched PubMed, Embase, and Cochrane databases to find randomized controlled trials (RCT) or observational studies published on April 16, 2015, and used dexmedetomidine with placebo or alternative anesthetics in patient comparing during CHD surgery. Their research lacks data to explain the effect of dexmedetomidine on cardiac complications [3]. Wang et al. believe that due to advances in the treatment and prevention of CHD, the mortality rate of cardiovascular diseases has decreased. He tried to determine the proportion of coronary heart disease patients who died from cardiovascular and noncardiovascular causes in a group of coronary heart disease patients, as well as the causes and predictors of death. During the 7680 person-year follow-up period, 401 people died. Although most of the mortality in their study was caused by noncardiovascular causes, the predictors of mortality are still unclear [4].

The patient takes a supine position and observes whether the target structure (left ventricular cavity) information is separated from the capture area during rotation, and the angle of the probe is adjusted to ensure that as much target structure information as possible can be obtained during 2D image acquisition. During the three-dimensional ultrasound sampling process, a total of 60 coaxial images were collected within the range of 180°, and the original data was stored in a SONY 2.6 GB readable and writable CD for offline three-dimensional reconstruction. To reflect the effect of virtual reality, it is necessary to provide users with interactive operation tools. Through these two methods, the effect of the basic virtual endoscope is realized. For example, the point of view can be placed in the heart, because the simulation occlusion must first find a suitable section to better observe and judge the occlusion effect, so this study uses the mouse interaction method to change the cutting by dragging and rotating the mouse position and normal direction of the surface, and then cut the three-dimensional volume data in any direction to find the best cut surface for the doctor to observe and diagnose. In the process of releasing the occluder, the parylene-coated occluder can be released after the X-ray and ultrasound examination results are satisfactory, and the delivery sheath and catheter can be sprinkled and compressed to stop bleeding.

2. Patient with Congenital Heart Disease

2.1. Parylene Material. Compared with traditional brushing, dipping, and spraying techniques, parylene material uses a unique vacuum vapor deposition polymerization process when forming a film, so the parylene series film has better antimold, antimoisture, and antisalt spray performance [5, 6]. During the film formation process, the parylene film monomer is directly sublimated into gas and then cracked. Without the intermediate state of the liquid phase, the cracked active small molecules directly form a polymer film on the surface of the substrate, which can be completely covered during the coating process. All shapes of objects, whether it is sharp edges, grooves, cracks, or inner surfaces, can be completely covered [7]. When the traditional solvent-based coatings are cured by the solvent, the coating thickness is uneven due to the volatilization of the solvent, and the discontinuity of the coating leads to many pinholes on the coating surface, and the air permeability and water permeability are high [8, 9]. Traditional coatings are prone to hydrolysis induced by water, because the polymer backbone of the parylene series of polymer films is all C, so parylene can avoid water-induced degradation and has better waterproof performance [10].

Compared with other traditional coating materials, parylene series films have many better properties. Since parylene was formally proposed in the 1960s, it has attracted the attention and research of researchers from all over the world. By introducing different substituents replaces the hydrogen atoms on the benzene ring to obtain different p-xylene monomers and obtain different parylene films with different physical and chemical properties, so that the parylene series films have a wider range of applications [7, 11]. Up to now, Union Carbide company has developed more than 20 kinds of parylene polymer materials, but due to use restrictions and environmental restrictions, there are currently three common commercial materials: ParyleneN film (parylene), ParyleneC film (poly P-xylene), and ParyleneD film (polydichloro-p-xylene) [9].

2.2. Interventional Closure of Atrial Septal Defect. Previous cardiac surgery is the only way to treat ASD [12, 13]. Minimally invasive interventional surgery is one of the hotspots in the medical field in recent years, especially the rapid development of cardiac interventional therapy. Because the adjacent relationship between the tissues around the atrial septum is relatively simple, the secondary hole ASD closure has been applied earlier in the clinic [14]. Early-developed occluders are likely to cause complications such as valve regurgitation and conduction block. At the same time, the incidence of residual shunts is relatively high, so their clinical application is limited. With the rapid development of minimally invasive interventional therapy for the heart, especially the double-disc nickel-titanium memory alloy occluder represented by the parylene occluder, it has introduced the closure of the secondary hole ASD in interventional therapy into a new field, providing patients with trauma. The new choice is of small size, good curative effect, and quick recovery. It is more acceptable to patients [15, 16].

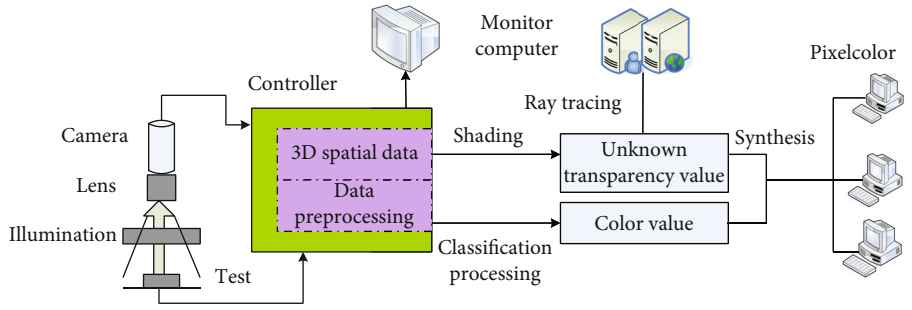

Figure 1: The flow of the ray casting method.

In the past, my country's occluders relied solely on foreign imports, and related standards and operations for blocking were simply imitated abroad. With the development and production of domestic double-disc nickel-titanium memory alloy occluders and the establishment of related domestic standards, not only the surgical cost is greatly reduced, and patient screening and related operations are more in line with China's national conditions, and now, it has been the first choice for the clinical application of ASD blocking interventional therapy for secondary holes [13].

2.3. Threshold Selection in 3D Visualization. In the two visualization methods of the three-dimensional data field, both are related to the problem of thresholds, such as the value of the median surface in surface rendering and the threshold t of the boundary between the target and the background in volume rendering [17, 18]. Due to the low resolution of ultrasound and the great influence of noise, it cannot be used as a threshold as a fixed value in CT or MRI images. Therefore, how to select the threshold value in 3D ultrasound visualization is a problem that must be solved [19].

Suppose that in the image f, the number of pixels whose gray value is$I$andn_1, and the total pixels are

$$N = \sum_{i=1}^{L} n_1. \tag{1}$$

The probability of each gray level is

$$p = \frac{n_1}{N}. \tag{2}$$

Suppose the image is divided into two regions with gray k as the threshold, then

$$\begin{aligned} \omega_A &= \sum_{i=1}^{k} p_i, \\ \omega_B &= \sum_{i=k+1}^{L} p_i. \end{aligned} \tag{3}$$

The average gray scale of regions A and B is

$$\begin{aligned} \mu_A &= \frac{1}{\omega} \sum_{i=1}^{k} i * p_i = \frac{\mu(k)}{\omega(k)}, \\ \mu_B &= \frac{1}{\omega} \sum_{i=k+1}^{L} i * p_i = \frac{\mu - \mu(k)}{1 - \omega(k)}. \end{aligned} \tag{4}$$

Among them, μ is the average gray level of the whole image,

$$\mu = \sum_{i=1}^{L} i * p_i = \omega_A \mu_A + \omega_B \mu_B. \tag{5}$$

The variance of the two regions is

$$\sigma^2 = \omega_A (\mu_A - \mu)^2 + \omega_B (\mu_B - \mu)^2 = \frac{\mu\omega(k) - \mu(k)}{\omega(k)(1 - \omega(k))}. \tag{6}$$

According to the criterion of maximum variance between classes, change L from 1 to K, and calculate the variance between classes, so that the maximum K of the above formula is the required threshold [20, 21].

2.4. Volume Rendering. Due to the complex structure of the heart and the high noise of ultrasound images, it is not realistic to classify simply by the original gray value of the data [22]. Thus, instead of using the commonly used piecewise function method to set the color value of the data, the value preprocessed by the original grayscale of each point is directly assigned to each point as its color value, so that the drawing can be more detailed. Since the main target to be visualized is the part with higher gray, the original gray value is relatively low, and the opacity of the background part is set to its gray value and divided by n, and the gray value is higher; set the partial opacity to 1. Through experiments, $n = 5$. Let the threshold for judging two cases bet. Using this method can appropriately reduce the impact of small deviations in the threshold set on the results. The flow of the ray casting method is shown in Figure 1. After the above process, the color value and transparency value of each sampling point where the light is projected are synthesized by a forward-to-back synthesis method to become the color of the pixel point, so the viewpoint can be in a certain

position or a certain direction. A three-dimensional ultrasound image of the heart is drawn [23, 24].

2.5. -Sided Drawing. In the 3D reconstruction of the surface rendering algorithm, because the reconstructed 3D surface mesh model is usually called by the isosurface, the 3D reconstruction process of the surface rendering algorithm is also called the process of isosurface extraction. The isosurface can be understood as having the same combination of gray pixels.

$$\{(x, y, z)|f(x, y, z) = c\}. \tag{7}$$

Among them, x, y, and z represent the coordinates corresponding to the sampling data points in the three-dimensional space. For the point whose subscript is (i, j, k), its gray value should be

$$Hu(i, j, k) = \text{scalars}(i, +jX + kXY). \tag{8}$$

Among them, scalars is the head pointer of the input data stream. For the point whose subscript is (i, j, k), its gray value should be

$$\text{Position}_{(i,j,k)} = (ia, jb, kc). \tag{9}$$

When rendering the triangle mesh model, to make the display of the model have a certain sense of reality and gloss, it is necessary to calculate the normal vector of the triangle. Assuming that the gradient value of the point (i, j, k) is (g_i, g_j, g_k), the central difference method using gray values is

$$\begin{aligned} g_i &= \frac{0.5\left(Hu_{(i+1,j,k)} - Hu_{(i-1,j,k)}\right)}{a}, \\ g_j &= \frac{0.5\left(Hu_{(i,j+1,k)} - Hu_{(i,j-1,k)}\right)}{b}, \\ g_k &= \frac{0.5\left(Hu_{(i,j,k+1)} - Hu_{(i,j,k-1)}\right)}{c}. \end{aligned} \tag{10}$$

When (i, j, k) is a boundary point, the cube whose subscript value differs by 1 may not exist. At this time, it needs to be replaced with its own gray value. For example, the gradient of the point$(0, j, k)$ in the i direction is

$$g_i = \frac{\left(Hu_{(1,j,k)} - Hu_{(1,j,k)}\right)}{a}. \tag{11}$$

2.6. Vision Sensor. In recent years, with the continuous development of computer vision and other technologies and increasingly convenient hardware devices such as vision sensors, the research on surgical detection based on vision sensors has been favored by increasing scholars. The vision sensor is developed on the basis of infrared vision navigation technology, and the vision system is mainly composed of binocular infrared cameras. During the operation, the vision sensor indirectly obtains the three-dimensional coordinates of the key physiological points of the knee joint through the sign and probe combined with the vision technology and determines the coordinate system of the cutting plane through the mathematical model. Finally, the robot completes the entire operation during the operation.

The depth information sensor selected in this article is XtionPROLIVE from ASUS, which uses USB to establish a connection with the data acquisition module, and is lighter than Microsoft's Kinect in size. The depth data information function of an Xtion camera is realized by its three sensing devices, from left to right are structured light transmitter, color camera, and infrared camera. Xtion is a depth information sensor that integrates many current advanced machine vision technologies. It can simultaneously obtain the RGB image from the current background and its corresponding depth information. The effective viewing distance of Xtion is 0.8 m-4.0 m, and the visualization angle of system imaging is 58° horizontally and 45°vertically. The price of Xtion is much lower than that of laser rangefinders, binocular vision equipment, etc., making it widely used and popularized. In addition, it can complete the synchronous acquisition of color images and depth information on the hardware, which greatly facilitates the research and development of users. Xtion has better real-time performance than other stereo vision equipment, and its color image data output can reach 30 frames per second. Therefore, this article uses Xtion equipment to complete the extraction of the key points of the heart.

3. Clinical Trials of a Patient with Congenital Heart Disease

3.1. Research Objects. In this study, 604 patients with congenital perimembranous ventricular septal defect who received VSD closure treatment were selected in the cardiology department of the hospital. Among them, there were 306 males and 298 females, aged 17.7 ± 13.4 (1~66) years old and weighing 41.8 ± 20.6 (9.5 ~ 97) kg. Before the operation, the congenital perimembranous ventricular septal defect was diagnosed by thoracic echocardiography (TTE) and left ventricular angiography. Among the 604 patients, 558 were with VSD alone, 17 with residual leakage after ventricular defect repair, and 29 with other malformations (including 17 with ASD, 9 with PDA, 1 with ASD+ pulmonary stenosis, 1 with ASD+PDA, and 1 with PDA+1 case of descending aorta coarctation). We classify pmVSD with a distance of less than 2 mm from the edge of the VSD to the aortic valve as a poor-margin VSD, and pmVSD with a distance ≥ 2 mm as a good margin VSD.

Exclusion criteria are simple VSD with abnormal hemodynamics and 3 mm < defect diameter < 14 mm; a small ventricular defect with a diameter of less than 3 mm without obvious hemodynamic abnormalities is a relative indication. For a porous ventricular septal defect with bulging tumor, the upper edge of the defect is more than 2 mm from the aortic valve as a relative indication. Intracranial ventricular septal defect is a relative indication.

3.2. Three-Dimensional Ultrasound Sampling. Under the operation state, patients under the age of 50 are given general anesthesia; under the nonoperation state, patients under the age of 30 are given a 10% chloral hydrate enema to make them fall asleep. The patient is in a supine position, a multiplanar transthoracic ultrasound probe is used, the four-chamber view is taken as the initial view, and the probe is rotated by 180° to observe whether there is any intracardiac target structure (left ventricular cavity) information that leaves the capture zone during rotation, and adjust the angle of the probe ensuring that as much target structure information as possible can be obtained when two-dimensional image acquisition. After that, the contact surface between the probe and the chest wall or abdominal wall remains unchanged, and the dynamic 3D acquisition program in the SONOS5500 integrated 3D data acquisition system is started, and the sampling angle interval is set to 3°, the image gain is 80%, and the image compression is 20%; start the heart electricity and respiration gating, use the ECG respiration monitoring function, monitor the ECG RR interval and the respiratory motion range for 1~2 min, set the allowable range of the ECG RR interval when the two-dimensional image information is acquired, and set a certain phase of breathing sampling. Then, start sampling and timing. In the meantime, within the range of 180°, a total of 60 coaxial section images were collected, and the original data were stored in a SONY 2.6 GB readable and writable CD for off-line 3D reconstruction.

3.3. ASD Three Interactive Virtual Reality Environment Establishment. In this study, an improved Marching Cube algorithm is used to implement an interactive virtual reality environment for the established three-dimensional data set. Cutting and observing any part of the heart are one of the essential means to assist doctors in diagnosis. In this study, the initial range was selected by the mouse interaction method, and then, the selected range was fine-tuned by changing the position of the slider and the profile.

In this article, to obtain the three-dimensional information of the key points of the heart, it is necessary to make RGB image information and depth information one-to-one correspondence. To make the depth information correspond to the color image, the image must be registered. Image registration is used to correspond the color image and the depth object, to generate the RGB-D image corresponding to each other pixels; that is, each pixel in the color image corresponds to the pixel in the depth image one to one. Xtion's image registration process is completed inside its PS1080 system-level chip, and all sensor information color images and depth images are transmitted to the user host through the USB interface.

To reflect the effect of virtual reality, it is necessary to provide users with interactive operation tools. This research provides two methods, mouse interaction and keyboard interaction. Through these two methods, the effect of the basic virtual endoscope is realized. For example, the point of view can be placed in the heart, because the simulation occlusion must first find a suitable section to better observe and judge the occlusion effect, so this study uses the mouse interaction method to change the cutting by dragging and rotating the mouse position and normal direction of the surface, and then cut the three-dimensional volume data in any direction to find the best cut surface for the doctor to observe and diagnose.

3.4. 3D Visualization of the Heart. After planning the path of each bone cutting plane, set the fitting speed and acceleration reasonably to better complete the cardiac data action and feedback of the remaining time to help doctors control the operation progress. The module mainly includes speed setting, acceleration setting, manipulator current state monitoring, cutting execution, emergency stop, and other functions.

When cutting the heart data, the essence is to use six faces to separate this part of the data from the data set. Therefore, using the data on these six faces to fill can not only play a role in repairing holes but can also be more delicate as the ground reflects the texture characteristics of the cut muscle. The surface rendering method realizes three-dimensional visualization by extracting the isosurface. For the ultrasound image of the heart, if the noise factor is not considered, the value of the isosurface is set to t; then, the part of the data with the gray value greater than t is the part of the myocardium. Therefore, the opacity of the data greater than t among all data on the six faces is 1, that is completely opaque, and the opacity of the data less than or equal to t is 0, that is, completely transparent. After the above improvements, the heart structure can be presented more clearly and more three-dimensionally.

The three-dimensional visualization of the heart is carried out using the method of surface rendering. Use volume rendering to visualize the atrial septal defect in three dimensions. Drag the slide bar on the interface to fine-tune the selection range, and through mouse interaction, you can select the appropriate section for easy observation. These methods can help doctors easily select the part of interest, perform virtual cuts on the heart, and see the details of the symptoms. The comparison of the parameters of the simulation device and the actual device is shown in Table 1.

3.5. Surgical Procedure

(1) Left and right cardiac catheterization and cardiovascular angiography: patients under 10 years old are under general anesthesia, ≥10-year old patients are under 2% lidocaine local anesthesia, puncture femoral artery and veins, place 5F-6F or 7F sheaths, routine heparin was given 100 U/kg, left and right cardiac catheterization was performed, pressure and blood oxygen were measured, pulmonary artery pressure and aortic and left ventricular pressure were measured, and the shape and size of the defect were displayed. At the same time, ascending aorta angiography was performed to observe for aortic valve prolapse and regurgitation

(2) Establish arterial and venous tracks: insert the right coronary angiography catheter from the femoral artery sheath to the left ventricle, the catheter enters the right ventricle through the VSD, and the exchange

Table 1: Comparison of parameters between the simulated device and the actual device.

Parameter	Parylene blocking device	Simulation device	P
Diameter of left atrium	30.70 ± 3.94 (22.65~37.18)	30.87 ± 4.49 (20.00~38.00)	0.441
Right atrium diameter	26.84 ± 3.95 (19.03~33.43)	27.00 ± 4.16 (18.00~34.00)	0.461
Distance from mitral valve	5.46 ± 2.79 (2.00~10.11)	5.26 ± 2.74 (1.73~9.49)	0.119
Distance from tricuspid valve	8.34 ± 2.88 (4.27~14.08)	8.17 ± 2.89 (3.98~13.96)	0.251

Table 2: ASD size of 2DE, 3DE, X-ray images, and measured values of the measuring board (mm).

Measurement methods	Measured value	P	r
X-ray image measurement	23.59 ± 8.82	<0.001	0.97
Two-dimensional ultrasonic measurement (upper and lower diameter)	19.65 ± 7.60	<0.001	0.97
Three-dimensional ultrasonic measurement (upper and lower diameter)	20.82 ± 7.43	<0.001	0.92
Two – dimensional ultrasound + balloon measurement	24.17 ± 7.94	>0.05	0.97
Measuring board value	24.45 ± 8.27	>0.05	0.98

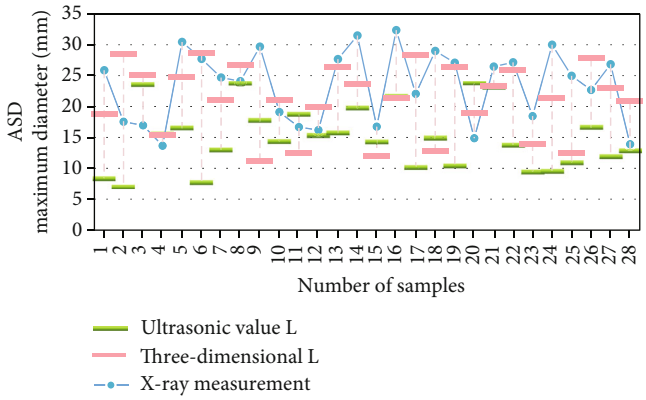

Figure 2: Comparison of ASD size measurement by three methods.

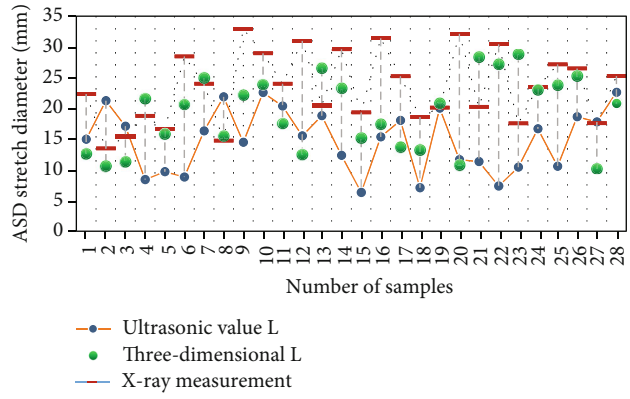

Figure 3: Comparison of two-dimensional ultrasound, X-ray images, and measurement board measured values after measuring balloon filling.

guide wire is sent through the catheter to the pulmonary artery or superior vena cava and then sent into the femoral vein. Insert the snare catheter and snare, wrap the guide wire, and pull it out of the body to establish the femoral vein-right atrium-right ventricle_VSD-left ventricle-aorta-femoral artery track

(3) Along the orbital guide wire, insert a suitable delivery sheath from the femoral vein end to the aorta, and slowly withdraw the sheath. Once the sheath is under the aortic valve, follow the guide wire and reach the apex of the left ventricle. The wire is used to send the sheath to the apex of the ventricle, and the guide wire and dilation tube are removed

(4) Placement of occluder: choose a suitable occluder according to the position and shape of the VSD. Connect the occluder to the delivery rod. Insert the delivery system through the delivery sheath, deliver the occluder to the end of the delivery sheath, release the left disc, retract the delivery sheath, and release the right disc. Transthoracic ultrasound, left ventricular angiography, and ascending aortic valve angiography were used to observe the position of the occluder, the presence or absence of shunt, and valve regurgitation

(5) Release occluder: parylene coated occluder can be released after the X-ray and ultrasound examination results are satisfactory, and the delivery long sheath and catheter can be compressed to stop bleeding

(6) Patients with ASD: VSD occlusion first, then ASD occlusion; for patients with PDA, PDA occlusion or

Table 3: Comparison of measured values of waist area before and after release of ASD and occluder (m^2).

ASD	Number	ASD color three-dimensional area	Occluder release front waist area	Waist area after occluder release
All ASD	30	4.06 ± 2.42	6.33 ± 3.48	3.96 ± 2.49
Circular ASD	8	2.45 ± 1.81	3.76 ± 2.11	2.34 ± 1.72
Noncircular ASD	22	4.65 ± 2.37	7.27 ± 3.44	4.55 ± 2.49

Table 4: Comparison of measured values of transthoracic two-dimensional and three-dimensional echocardiography (cm).

ASD	Number	Large-vessel short-axis inner diameter	Three-dimensional maximum inner diameter	Occluder release front waist area	Waist diameter after occluder release
All ASD	30	1.91 ± 0.68	2.45 ± 0.82	2.71 ± 0.85	2.12 ± 0.76
Circular ASD	8	1.49 ± 0.62	1.74 ± 0.71	2.10 ± 0.66	1.61 ± 0.65
Noncircular ASD	22	2.06 ± 0.65	2.71 ± 0.71	2.93 ± 0.82	2.30 ± 0.73

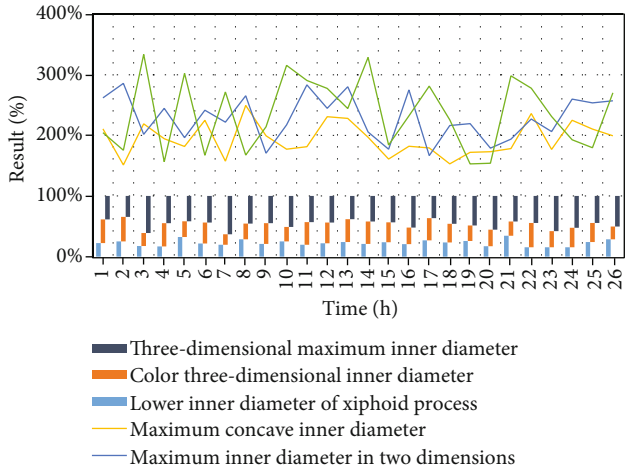

Figure 4: Comparison of measured values of transthoracic two-dimensional and three-dimensional echocardiography.

VSD occlusion first: for PS, pulmonary valvuloplasty (PBPV) is performed first

4. Clinical Efficacy of Congenital Heart Disease in Patients

4.1. 3D Reconstruction Analysis. In this group of patients, 29 cases were sampled by TEE (transesophageal echocardiography), 14 cases were sampled by TTE (transthoracic echocardiography), and 23 cases of TEE were successful in both preoperative and postoperative three-dimensional reconstruction (reconstruction success rate 79%, 23/29) and 11 cases of TTE (reconstruction success rate 79%, 11/14). The ASD size measured by different methods in 34 patients with successful 3D reconstruction was counted. The results showed that the upper and lower diameters of the ASD measured by two-dimensional ultrasound before the operation were 19.65 ± 7.60 mm, and the anteroposterior diameter was 16.03 ± 6.64 mm; the upper and lower diameters of the ASD measured by the three-dimensional ultrasound were 20.82 ± 7.43 mm, and the anterior and posterior diameters were 18.16 ± 7.07 mm; balloon filling was measured during the operation. The upper and lower diameters of the ASD measured by the posterior two-dimensional ultrasound were 24.17 ± 7.94 mm, and the front and rear diameters were 21.30 ± 6.54 mm; the ASD size measured by X-ray imaging was23.59 ± 8.82 mm; the ASD size measured by the measuring board was 24.45 ± 8.27 mm. For patients with minimal residual shunt after surgery, clinical follow-up can be done to observe whether the residual shunt is aggravated. We believe that the residual shunt below 3 mm has a good prognosis and can be treated without treatment. Oral antibiotics can be used to prevent infective endocarditis; for moderate to large residual shunt patients, if the shunt volume is greater than 5 mm, surgical intervention is required, which can be blocked again or transferred to surgical repair. The 2DE, 3DE, X-ray images, and measurement values (mm) of the ASD size are shown in Table 2. The comparison of the three methods for the ASD size measurement is shown in Figure 2. Figure 3 shows the comparison of two-dimensional ultrasound, X-ray images, and the measured values of the measuring board after the balloon is filled [25].

Two of the 11 patients with cAVB (complete atrioventricular block) had I-degree atrioventricular block when the catheter was pushed during the operation, and recovered after 10 minutes of stopping the operation and completed the occlusion treatment without recurring conduction block stagnant. Nine patients developed cAVB on postoperative ECG monitoring, all accompanied by dizziness or syncope. One patient returned to normal after chest compression and hormone therapy, one patient returned to normal after only hormone therapy, and five patients were temporarily placed. For cardiac pacemakers, 2 cases had permanent cardiac pacemakers. Among the 2 patients with permanent cardiac pacemakers, 1 patient had a history of repeated amaurosis and syncope before the closure operation, and the 24-hour Holter examination showed a transient second-degree atrioventricular block, which was repeated 7 days after the operation hemorrhage appeared, second-degree cAVB appeared again, and pacemaker placement was performed. The other patient was a VSD+ASD patient, who had first-degree AVB+RBBB postoperatively. After symptomatic treatment, first-degree cAVB disappeared, and second-degree cAVB appeared after one month. Permanent pacemaker

Table 5: Left ventricular volume change.

Parameter Time	LVEDV (ml)	LVESV (ml)	EF (%)
Preoperative	77.83 ± 19.62	18.22 ± 3.12	75.78 ± 4.41
Immediately after surgery	77.06 ± 18.24	18.50 ± 2.85	75.28 ± 4.16
3 days after surgery	60.50 ± 13.49	18.17 ± 2.94	69.44 ± 4.95

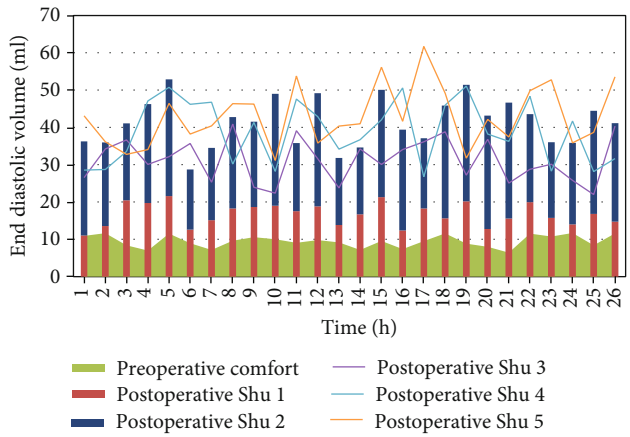

Figure 5: Changes of LVBDV before and after VSD closure.

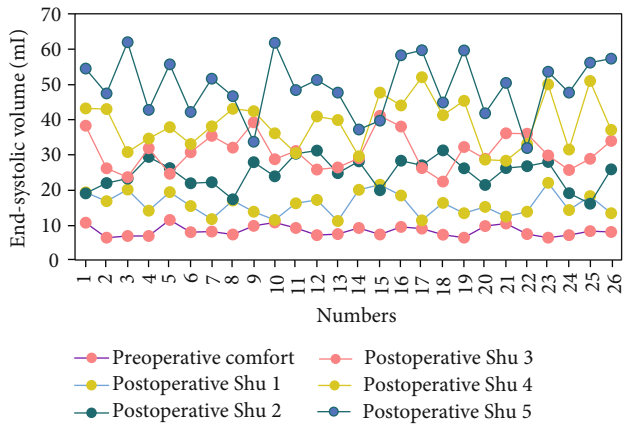

Figure 6: Changes of LVESV before and after VSD closure.

placement was performed. Therefore, only 1 case of permanent pacemaker was installed due to occlusion. The median time for cAVB in 9 patients was 5 days after surgery. The comparison (m^2) of the measured values of the waist area before and after the release of the ASD and the occluder is shown in Table 3. The comparison of the measured values of transthoracic two-dimensional and three-dimensional echocardiography (cm) is shown in Table 4. The comparison of the measured values of transthoracic two-dimensional and three-dimensional echocardiography is shown in Figure 4.

4.2. Left Ventricular Volume Analysis. Before and after the operation, the volume of the left ventricle had a significant change, and the volume after the operation was significantly reduced. The results of the study showed that the left ventricular volume and ejection fraction immediately after the closure were not significantly different from those before the operation, but the end-diastolic volume was significantly reduced 3 days after the operation, and the end-systolic volume remained unchanged. The ejection fraction also decreased, but within the normal range. It is suggested that with the closure of VSD, the left-to-right shunt at the ventricular level is blocked, the left ventricular volume load is reduced, and the enlarged left ventricular cavity is restored early after treatment, while the left ventricular systolic function has little effect. The changes in left ventricular volume are shown in Table 5. Figure 5 shows the changes of LVBDV before and after VSD blocking. The change of LVESV before and after VSD closure is shown in Figure 6. Figure 7 shows the change of EF before and after VSD closure.

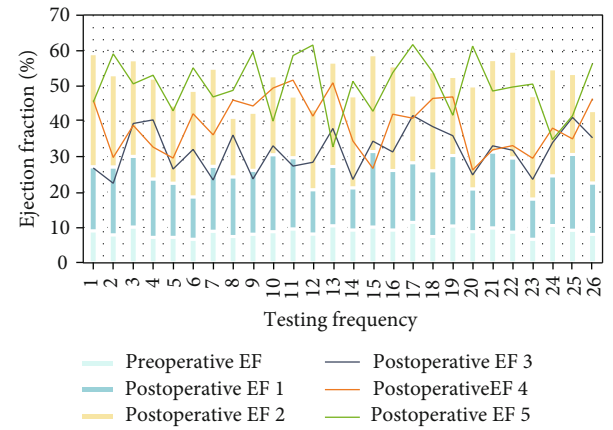

Figure 7: Changes of EF before and after VSD closure.

4.3. Valve Regurgitation Analysis. The situation of valve regurgitation is shown in Table 6. Intraoperative aortic angiography showed that 20 patients had microsmall aortic regurgitation, and 1 case had moderate aortic regurgitation. After the occluder was placed during the operation, the aortic regurgitation was not aggravated by aortic angiography. Postoperative reexamination of cardiac color Doppler ultrasound revealed that 11 of these 20 patients with aortic regurgitation had disappeared regurgitation, and a total of 5 patients had aortic regurgitation aggravated, of which 3 cases were aggravated with a small amount of preoperative regurgitation. Univariate analysis results showed that age, weight, and new aortic regurgitation are related, and there are significant differences. The results of multivariate logistic analysis showed that aortic regurgitation had nothing to do with the type of occluder, VSD location, and VSD shape. In 2 patients, there was a moderate to large amount of tricuspid

Table 6: Valve regurgitation.

Index (unit)	No regurgitation	Main valve regurgitation	P
Age	17.38 ± 13.1 1	41.4 ± 13.61	0.0000
Weight (kg)	41.99 ± 20.65	60.14 ± 5.84	0.0002
Pulmonary artery pressure measurement (mmHg)	11.95 ± 8.39	20.24 ± 6.12	0.4390
Operation time (min)	50.37 ± 30.27	59.78 ± 24.15	0.2947
Occluder-VSD diameter (mm)	2.26 ± 2.03	3.04 ± 2.12	0.0662

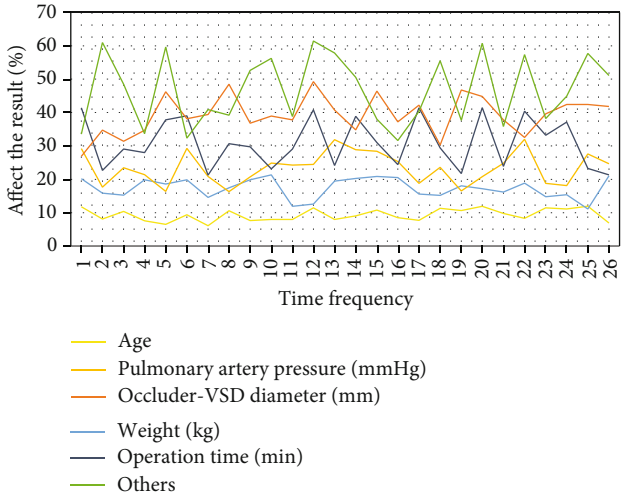

Figure 8: Different factors affect the results.

regurgitation before the operation. After successful closure, the reexamination of cardiac color Doppler ultrasound tricuspid regurgitation reduced at least the amount of regurgitation. Postoperative cardiac color Doppler ultrasound newly discovered 32 cases of microsmall amount of tricuspid regurgitation and 3 cases of moderate amount of regurgitation. One patient who gave up occlusion had hemolysis and a large amount of tricuspid regurgitation after the operation. The occluder was removed by intervention again, and the tricuspid regurgitation was rechecked. There was no massive tricuspid regurgitation in patients who were successfully blocked. Statistical analysis of tricuspid regurgitation has no related factors; the reasons are considered related to the location of the ventricular defect, operation damage, and the impact of tricuspid valve opening and closing after occluder implantation. Therefore, it is necessary to avoid damaging the tricuspid valve and chordae during the establishment of the orbit. Ultrasound detection should be performed during the operation. If obvious tricuspid regurgitation is found, the occlusion treatment should be abandoned. No other valve regurgitation that significantly worsened was found. The results of different factors are shown in Figure 8.

5. Conclusion

In this study, an improved Marching Cube algorithm is used to implement an interactive virtual reality environment for the established three-dimensional data set. Cutting and observing any part of the heart is one of the essential means to assist doctors in diagnosis. In this study, the initial range was selected by the mouse interaction method, and then, the selected range was fine-tuned by changing the position of the slider and the profile. Connect the occluder to the delivery rod. Insert the delivery system through the delivery sheath, deliver the occluder to the end of the delivery sheath, release the left disc, retract the delivery sheath, and release the right disc. Transthoracic ultrasound, left ventricular angiography, and ascending aortic valve angiography were used to observe the position of the occluder, the presence or absence of shunt, and valve regurgitation.

To reflect the effect of virtual reality, it is necessary to provide users with interactive operation tools. This research provides two methods, mouse interaction and keyboard interaction. Through these two methods, the effect of the basic virtual endoscope is realized. For example, the point of view can be placed in the heart, because the simulation occlusion must first find a suitable section to better observe and judge the occlusion effect, so this study uses the mouse interaction method to change the cutting by dragging and rotating the mouse position and normal direction of the surface, and then cut the three-dimensional volume data in any direction to find the best cut surface for the doctor to observe and diagnose.

When cutting the heart data, the essence is to use six faces to separate this part of the data from the data set. Therefore, using the data on these six faces to fill can not only play a role in repairing holes but can also be more delicate as the ground reflects the texture characteristics of the cut muscle. The surface rendering method realizes three-dimensional visualization by extracting the isosurface. After the above improvements, the heart structure can be presented more clearly and more three-dimensionally. The three-dimensional visualization of the heart is carried out using the method of surface rendering. Use volume rendering to visualize the atrial septal defect in three dimensions. These methods can help doctors easily select the part of interest, perform virtual cuts on the heart, and see the details of the symptoms.

Data Availability

Data sharing is not applicable to this article as no datasets were generated or analyzed during the current study.

Conflicts of Interest

The authors declare that there are no conflicts of interest regarding the publication of this article.

Authors' Contributions

Hongdu Fu and Liming Liang contributed equally to this work as co-first authors.

Funding

This work was supported by 16A200018.

References

[1] S. A. Brown, H. Jouni, T. S. Marroush, and I. J. Kullo, "Disclosing genetic risk for coronary heart disease: attitudes toward personal information in health records," *American Journal of Preventive Medicine*, vol. 52, no. 4, pp. 499–506, 2017.

[2] S. Purnima and B. G. A. El-Aal, "Ácido urico sanguineo como marcador pronostico de cardiopatia coronaria," *Clínica e Investigación en Arteriosclerosis*, vol. 28, no. 5, pp. 216–224, 2016.

[3] W. Pan, Y. Wang, L. Lin, G. Zhou, X. Hua, and L. Mo, "Outcomes of dexmedetomidine treatment in pediatric patients undergoing congenital heart disease surgery: a meta-analysis," *Paediatric Anaesthesia*, vol. 26, no. 3, pp. 239–248, 2016.

[4] E. Y. Wang, J. Dixson, N. B. Schiller, and M. A. Whooley, "Causes and predictors of death in patients with coronary heart disease (from the heart and soul study)," *The American Journal of Cardiology*, vol. 119, no. 1, pp. 27–34, 2017.

[5] M. D. DeBoer, M. J. Gurka, S. H. Golden et al., "Independent associations between metabolic syndrome severity and future coronary heart disease by sex and race," *Journal of the American College of Cardiology*, vol. 69, no. 9, pp. 1204-1205, 2017.

[6] M. Cantinotti, I. Valverde, and S. Kutty, "Three-dimensional printed models in congenital heart disease," *The International Journal of Cardiovascular Imaging*, vol. 33, no. 1, pp. 137–144, 2017.

[7] Y. Kubota, H. Iso, N. Sawada, S. Tsugane, and The JPHC Study Group, "Association of breakfast intake with incident stroke and coronary heart disease," *Stroke*, vol. 47, no. 2, pp. 477–481, 2016.

[8] X. M. He, L. Chen, T. S. Wang, Y. B. Zhang, J. B. Luo, and X. X. Feng, "E670G polymorphism of _PCSK9_ gene of patients with coronary heart disease among Han population in Hainan and three provinces in the northeast of China," *Asian Pacific Journal of Tropical Medicine*, vol. 9, no. 2, pp. 172–176, 2016.

[9] R. Noguchi, K. Nakayama, M. Itoh et al., "Development of a three-dimensional pre-vascularized scaffold-free contractile cardiac patch for treating heart disease," *The Journal of Heart and Lung Transplantation*, vol. 35, no. 1, pp. 137–145, 2016.

[10] E. A. Bohula, M. P. Bonaca, E. Braunwald et al., "Atherothrombotic risk stratification and the efficacy and safety of vorapaxar in patients with stable ischemic heart disease and previous myocardial infarction," *Circulation*, vol. 134, no. 4, pp. 304–313, 2016.

[11] J. Jiang, Y. Chen, J. Shi, C. Song, J. Zhang, and K. Wang, "Population attributable burden of Helicobacter pylori-related gastric cancer, coronary heart disease, and ischemic stroke in China," *European Journal of Clinical Microbiology & Infectious Diseases*, vol. 36, no. 2, pp. 199–212, 2017.

[12] U. N. Das, "Heart-type fatty acid-binding protein (H-FABP) and coronary heart disease," *Indian Heart Journal*, vol. 68, no. 1, pp. 16–18, 2016.

[13] L. J. Shaw, L. M. Phillips, E. Nagel, D. E. Newby, J. Narula, and P. S. Douglas, "Comparative effectiveness trials of imaging-guided strategies in stable ischemic heart disease," *JACC: Cardiovascular Imaging*, vol. 10, no. 3, pp. 321–334, 2017.

[14] S. M. Ford, M. T. McPheeters, Y. T. Wang et al., "Increased regurgitant flow causes endocardial cushion defects in an avian embryonic model of congenital heart disease," *Congenital Heart Disease*, vol. 12, no. 3, pp. 322–331, 2017.

[15] P. D. Morton, N. Ishibashi, and R. A. Jonas, "Neurodevelopmental abnormalities and congenital heart disease," *Circulation Research*, vol. 120, no. 6, pp. 960–977, 2017.

[16] M. M. Gevorgyan, N. P. Voronina, N. V. Goncharova et al., "Cystatin C as a marker of progressing cardiovascular events during coronary heart disease," *Bulletin of Experimental Biology & Medicine*, vol. 162, no. 4, pp. 421–424, 2017.

[17] D. G. Wilson, M. Zeb, G. Veldtman, B. D. Dimitrov, and J. M. Morgan, "Left and right parasternal sensing for the S-ICD in adult congenital heart disease patients and normal controls," *Pacing and Clinical Electrophysiology*, vol. 39, no. 3, pp. 282–290, 2016.

[18] Z. Fatmi and D. Coggon, "Coronary heart disease and household air pollution from use of solid fuel: a systematic review," *British Medical Bulletin*, vol. 118, no. 1, pp. 91–109, 2016.

[19] H. M. Ahmed, M. Miller, K. Nasir et al., "Primary low level of high-density lipoprotein cholesterol and risks of coronary heart disease, cardiovascular disease, and death: results from the multi-ethnic study of atherosclerosis," *American Journal of Epidemiology*, vol. 183, no. 10, pp. 875–883, 2016.

[20] Y. Wang, H. Y. Cao, M. X. Xie et al., "Cardiovascular cast model fabrication and casting effectiveness evaluation in fetus with severe congenital heart disease or normal heart," *Journal of Huazhong University of ence and Technology Medical ences*, vol. 36, no. 2, pp. 259–264, 2016.

[21] C. J. Mcleod and C. Warnes, "Recognition and management of arrhythmias in adult congenital heart disease," *Current Opinion in Cardiology*, vol. 31, no. 1, pp. 117–123, 2016.

[22] J. Liao, X. Guo, M. Wang et al., "Scavenger receptor class B type 1 deletion led to coronary atherosclerosis and ischemic heart disease in low-density lipoprotein receptor knockout mice on modified western-type diet," *Journal of Atherosclerosis & Thrombosis*, vol. 24, no. 2, pp. 133–146, 2017.

[23] A. Rick, M. D. Nishimura, and MACC, FAHA Writing Group Member, "AHA/ACC focused update of the 2014 AHA/ACC guideline for the management of patients with valvular heart disease: a report of the American College of Cardiology/American Heart Association task force on clinical practice guidelines," *Journal of the American College of Cardiology*, vol. 70, no. 2, pp. 252–289, 2017.

[24] J. C. L. Rodrigues, S. Rohan, A. Ghosh Dastidar et al., "Hypertensive heart disease versus hypertrophic cardiomyopathy: multi-parametric cardiovascular magnetic resonance discriminators when end-diastolic wall thickness ≥15 mm," *European Radiology*, vol. 27, no. 3, pp. 1125–1135, 2017.

[25] Z. Xu, D. Shi, and Z. Tu, "Research on diagnostic information of smart medical care based on big data," *Journal of Healthcare Engineering*, vol. 2021, Article ID 9977358, 10 pages, 2021.